Modeling Acoustical Pressure and Particle Acceleration Close to Marine Seismic Airguns and Airgun Arrays

Prior, Mark K.; Duncan, Alexander J.; Sertlek, Ozkan; Ainslie, Michael A.

DOI
10.1109/JOE.2019.2891873

Publication date
2019

Document Version
Final published version

Published in
IEEE Journal of Oceanic Engineering

Modeling Acoustical Pressure and Particle Acceleration Close to Marine Seismic Airguns and Airgun Arrays

Mark K. Prior, Alexander J. Duncan, H. Özkan Sertlek, and Michael A. Ainslie

***Abstract*—Comparisons are made of sound pressure and particle acceleration predicted by two methods in the vicinity of two arrays of marine-seismic airguns. Data describing the array properties and the environmental conditions are taken from test cases designed to facilitate intermodel comparison. The two propagation approaches, one based on method of images and the other on wave number integration, are shown to be capable of giving line-on-line agreement when the latter method implements the full form of the Hankel transform; when the more approximate Fourier transform is used, predictions are shown to differ at ranges of a few meters from the source.**

***Index Terms*—Acoustic propagation, airgun, particle acceleration, pressure waveform, marine-seismic.**

I. Introduction

INCREASING societal concern about the impact of underwater sound on marine life has led to the development of regulations regarding acceptable levels of sound that may be radiated or transmitted during seagoing industrial activities, including marine seismic surveys. These regulations can require that initiators of underwater sound demonstrate that acoustical levels are within acceptable limits. At-sea monitoring of sound levels is complex and expensive and it would be beneficial if a modeling capability could be developed so that levels could be accurately predicted before the start of sound-generating activities. Models exist to describe the generation and propagation of underwater sound and it is important that their suitability for use is demonstrated by validation of their predictions against reference solutions.

Comparison of model predictions against experimental measurements is an important part of any validation process. However, a model-measured comparison only represents a meaningful test of a model's capability if the measurements and processing are fully calibrated and detailed environmental data were gathered during the acquisition of the acoustical data. Any uncertainty in calibration leads to uncertainty in the acoustical field against which the model predictions are to be compared. Insufficient environmental information often prevents the situation under study being described to the model to a level of detail sufficient to provide a test of the model's capabilities. While data sets suitable for airgun signature model validation studies exist they are limited either to single airguns (or clusters) [1] or to the precise equipment configurations and environmental conditions predominant during the data acquisition [2].

While comparison with measured data is always desirable, important information regarding model capabilities can be obtained in the absence of measured data by model–model comparisons in well-characterized test cases [3], [4]. In these test cases, the environment may be specified precisely, removing the problems associated with incomplete environmental information that can occur with model–measurement comparisons. In some cases, it may be possible to derive precise solutions to hydrodynamic and wave equations and these solutions represent "benchmarks" for a specified scenario. The departure of any model's prediction from these benchmarks can be considered a measure of that prediction's error in this scenario. In the absence of a trusted benchmark, useful insights into the validity of model assumptions may still be obtained by comparison between the predictions of different models. Models produce their results via different techniques, each subject to particular approximations. If two models based on different approaches produce the same predictions in a well-specified test case, then the models' predictions are mutually consistent, increasing confidence in both. There remains the possibility that two models may make the same mistake and predict the same erroneous value. However, the risk of this occurring is reduced if the models are based on approaches subject to different types of approximation. Thus, if a model based on approximations that assume low frequency and short range makes predictions that agree with one based on approximations that assume high frequency and long range, it may reasonably be stated that any agreement at intermediate frequencies and ranges provides support for their mutual validity in that intermediate regime.

To improve confidence in current modeling capabilities for sound fields generated by marine-seismic airguns, a series of test cases has been developed [5]. These cases include descriptions of the ocean environment and airgun arrays. The environmental

Manuscript received April 30, 2018; revised November 23, 2018; accepted December 21, 2018. Date of publication January 31, 2019; date of current version July 12, 2019. *(Corresponding author: Mark K. Prior.)*

Guest Editor: K. Heaney.

M. K. Prior is with the Acoustics and Sonar Department, TNO, The Hague 2597, The Netherlands (e-mail: mark.prior@tno.nl).

A. J. Duncan is with the Centre for Marine Science and Technology, Curtin University, Bentley, WA 6102, Australia (e-mail: A.J.Duncan@curtin.edu.au).

H. Ö. Sertlek is with the Faculty of Civil Engineering and Geosciences, Delft 102628, The Netherlands, and also with the Department of Electronics Engineering, Gebze Technical University, Gebze 41400, Turkey (e-mail: osertlek@gmail.com).

M. A. Ainslie is with the JASCO Applied Sciences (Deutschland) GmbH, Eschborn 65760, Germany (e-mail: michael.ainslie@jasco.com).

Digital Object Identifier 10.1109/JOE.2019.2891873

description data they use are based on similar descriptions used in test cases designed for assessing the validity of models used to predict the performance of sonars [3]. They represent a common ground in which two types of model may be run and compared:

1) models describing the production of sound by airgun arrays;
2) models describing the propagation of sound from arrays to receivers.

This paper describes a comparison of two models that predict the propagation of sound from airguns to nearby receivers. Both approaches use the same source description but employ different approximations in their propagation modeling to convert from the time-domain source waveform to the sound pressure time series at the receiver. One approach is based on the method of images by which propagation from source to receiver is combined with propagation from the image of the source associated with reflection from the sea surface and whose pressure signal is inverted in sign due to the pressure-release boundary condition imposed at the air–water interface. The second approach is more sophisticated and is based on a wavenumber integration technique [6]. The method of images provides an accurate solution shortly after transmission and at locations close to the array where the direct and surface-reflected paths are the only valid routes by which sound can get from source to receiver, thus providing a valuable check in this regime on wavenumber integration predictions. The wavenumber integration method is potentially valid over a much larger spread of times and source-receiver ranges. A comparison of the two methods therefore represents an effective investigation of their validity.

In addition to the sound pressure, a measure of particle motion is also needed. This type of descriptor of the acoustical field is particularly relevant to applications associated with the impact of underwater sound on marine life because taxa such as crustaceans and fishes are thought to sense particle motion (particularly particle acceleration) rather than acoustical pressure [7]. The simple far-field relation between the two does not exist in all cases, e.g., close to the source or close to a reflecting boundary.

Comparisons are made in terms of predictions of sound pressure and particle acceleration. To satisfy the assumptions made in the derivation of the two methods, calculations are restricted to receiver locations close to the center of two arrays of marine-seismic airguns. Source array and environmental data are taken from test cases developed for the purpose of model validation [8].

Section II describes the test cases in terms of source and environment descriptions while Section III describes the source model used to produce the source waveform for the two approaches. The propagation models used by the two approaches are described in Section IV and results are presented in Section V. Finally, Section VI and Section VII provide the summary and conclusion, respectively, of this paper.

II. Test Case Specifications

A. General

Test cases were designed to represent a complete specification of the acoustical problem that must be solved to predict the acoustical field in an underwater environment in which marine-seismic airguns operate. Such a specification requires details of the airguns and the environment. These two areas are described in Sections II-B and II-C.

TABLE I
Environmental Properties

Parameter	Value	Unit
Hydrostatic pressure at 5 m	0.152	MPa
Wind Speed	0	m/s
Seawater Temperature	10	°C
Seawater Sound Speed	1500	m/s
Seawater Density	1000	kg/m^3
Seawater Acoustical absorption	Frequency dependent, based on the equation by Thorp [9]	Nepers/m
Seabed type	Fluid sand homogenous half-space	-
Seabed Sound Speed	1700	m/s
Seabed Density	2000	kg/m^3
Seabed Absorption	0.5	dB per acoustical wavelength
Water depth	50	m

B. Environment

The propagation medium considered was representative of a shallow-water environment with 50 m of seawater overlying a sandy seabed. It was based on an environment previously used for validation of sonar-performance models [3]. Not all models are capable of using the full environmental description data and some, for example, have their own internal model of seawater attenuation. For the study reported here, only those parameters were used which could be input to both propagation models. Description data are given in Table I. Parameters which were not used are indicated by gray text.

C. Sources

Two sources were considered, comprising a subset of those described in the test cases [5]. source 1 represented the simplest case of a single airgun deployed at a depth of 5 m. The airgun was specified in terms of its manufacturer and model type and a chamber pressure. source 2 represented a single line array of airguns of various models and volumes, all fired at the same time and with the same chamber pressure. Details are given in Table II with (x, y, z) locations described in terms of right-handed Cartesian axes with origin at the sea surface and with (positive) depth increasing downwards.

The data in Table II describe powerful acoustical sources and it is possible that the pressure fluctuations that they cause may represent a significant fraction of the ambient pressure at their deployment depths. With such large departures from ambient pressure, it is possible that the assumptions of linear acoustics may no longer be valid. However, the work reported here is restricted to an assumption of linear acoustics. In this sense, a solution is provided to a well-posed mathematical problem but there remains a question regarding how well that solution fits the physics of the situation. An investigation of the consequences of any potential nonlinearities is outside the scope of the work reported here.

TABLE II
SOURCE PROPERTIES

	x/ m	y/ m	z/ m	Airgun Type	Volume		Operating over-pressure	
					L	in^3	MPa	lbf/in^2
Source 1								
	0	0	5	Bolt 1500LL 155	2.540	155	13.790	2000
Source 2								
	+6	0	5	Bolt 1500LL 480	7.866	480	13.790	2000
	+3	0	5	Bolt 1500LL 290	4.752	290	13.790	2000
	0	0	5	Bolt 1500LL 155	2.540	155	13.790	2000
	-3	0	5	Bolt 1900LLX 200	3.277	200	13.790	2000
	-6	0	5	Bolt 1900LLX 100	1.639	100	13.790	2000
	-9	0	5	Bolt 1900LLX 90	1.475	90	13.790	2000

Operating overpressure is the airgun pressure relative to the atmospheric pressure.

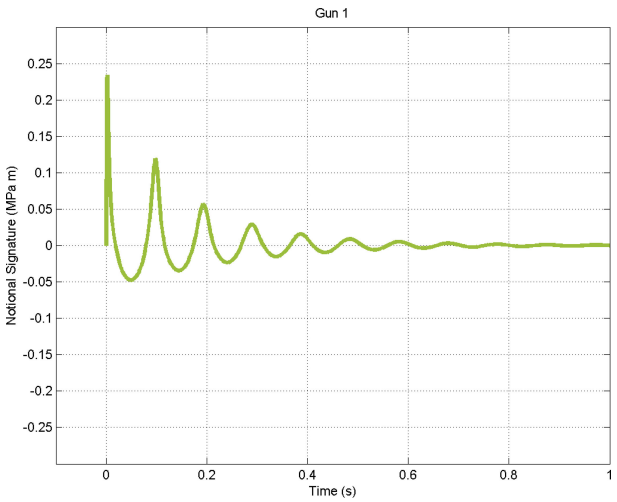

Fig. 1. Source waveform for source 1 (single airgun).

III. AIRGUN SOURCE MODEL: AGORA-2

The data in Table II were used to produce an acoustical description of each source. This description took the form of a source waveform [10], sometimes referred to as a "notional signature" and being the product of distance and sound pressure in the acoustical far-field of a sound source in a hypothetical, infinite, uniform, lossless medium with the same acoustical properties as the seawater in Table I. The dimensions of the "source waveform," which is a function of time, are pressure times distance. An example of waveform for source 1 is shown in Fig. 1.

The source waveform of each airgun source was calculated using the AGORA computer code [11]. This model initially considers each airgun separately and solves differential equations to give the motion of a bubble formed by the given volume of air injected at the given chamber pressure. The bubble motion is then modified in a first-order perturbative approach that takes into account the effect of other bubbles. This perturbation allows for the fact that the motion of the bubble wall is affected by pressure fields radiated by neighboring bubbles and by surface-reflected waves from bubbles, including itself. This means that the source waveforms produced by AGORA include the influence of the surface-reflected wave on the motion of the bubble but do not include that wave itself. This surface reflection, also known as the "surface ghost," is a propagation effect that should be included in the propagation model.

The bubble of air released at high pressure by the airgun undergoes a series of expansions and contractions, resulting in a corresponding sequence of compressions and rarefactions in the surrounding water. These density changes propagate into the bubble's far field, and manifest themselves as a series of positive and negative peaks in the source waveform. This process is not loss free and the amplitudes of successive peaks in the signature decrease as the system loses energy to radiative and dissipative processes.

The time between the peaks in the source waveform caused by the initial injection and the first bubble collapse is determined by the operating chamber pressure, deployment depth, and volume of the airgun. Arrays of airguns are designed so that the secondary peaks in their signatures occur at different times while their initial injections are usually synchronized. This is done to produce a strong, single initial peak with destructive interference between airguns and surface-reflected paths reducing the amplitude of subsequent peaks.

The AGORA-2 model includes the possibility of summing source waveforms for individual airguns to produce a far-field time-domain array signature as a function of vertical and horizontal angle. However, this was not done in this study. Instead, source waveforms from individual airguns were considered separately and their pressures summed coherently at the points of interest after propagation. This was done because the model-comparison process was carried out at distances from the array that were small compared to its dimension and the validity of the far-field criterion was questionable.

IV. PROPAGATION

A. General

The source waveform may be combined with a transfer function describing propagation between source and receiver to produce a sound pressure signal at a receiver. In the case of a homogenous environment, this transfer function amounts to a delay and a division by the range between source and receiver. In more complicated environments, a more sophisticated model is required but the transfer function retains dimensions of L^{-1}.

The test case specification [5], [8] provided a list of output options in terms of acoustical field variables and receiver locations at which these should be produced. The work reported here considers a subset of these, namely sound pressure and sound particle acceleration calculated at horizontal offsets of 3 and 30 m.

B. Method of Images

In the first method, the total sound pressure at a point was modeled as the sum of the contributions from direct and surface-reflected paths [12], [6]. The direct path results in a contribution

to the sound pressure equal to the source waveform divided by the direct path distance. The surface-reflected path makes a similar contribution but the source waveform is inverted to allow for the fact that the sea surface has a pressure-reflection coefficient of -1. The sound pressure p_j at a point (x_r, y_r, z_r) is therefore a function of time given by

$$p_j\left(x_r, y_r, z_r, t\right) = \frac{s_j\left(t - \frac{r_{d,j}}{c_w}\right)}{r_{d,j}} - \frac{s_j\left(t - \frac{r_{s,j}}{c_w}\right)}{r_{s,j}} \quad (1)$$

where subscript *r* denotes the receiver position, subscript *d* refers to the direct path, subscript *s* is the surface-reflected path, c_w is the seawater sound speed, and $s_j(t)$ is the source waveform of the *j*th airgun in the source array. The ranges are given by straight-line geometry. The total sound pressure at a point is the sum over *j* of the contributions of all airguns.

The simplicity of the method of images was deliberately chosen so that the predictions would form a baseline case against which more sophisticated propagation models could be compared. The predictions of the method of images can be straightforwardly understood and the reasons for features observed in the data explained. More sophisticated models employing numerical solution methods provide answers that may be precise but which have no physical insight that helps to interpret them. Thus, a change in the gradient of pressure with time predicted by a sophisticated model might be due to the arrival of the surface-reflected wave or it may be a consequence of a numerical error in the model's formulation. Comparison between the predictions of sophisticated models and the method of images thus allows insight to be obtained as to the physical processes underlying some of the features that might be observed in model predictions.

The simplicity of the method of images results in it being subject to significant limitations of applicability. The contributions of the two paths take the form of time-shifted and amplitude-scaled versions of the nominal airgun signatures. This neglects the effects of dispersion and deformation of the signal that may take place along those single paths due, for example, to frequency-dependent attenuation.

This implementation of the method of images also neglects contributions other than the direct and surface-reflected paths. Although the method can be extended to include seabed reflected paths and paths involving multiple seabed and surface reflections [12], [6] the complexities of dealing with the reflection of a low-frequency spherical wave from a realistic seabed [13] would negate the method of images' advantage of simplicity and is not needed at close proximity to the source. The test-case environment included a seabed and reflections from this contribute to the acoustical field at times greater than the travel time from source to seabed to receiver. The method will therefore be accurate at the short times in which absorption and the contribution of seabed-reflected paths may be neglected.

In addition to sound pressure, particle motion was also considered in the form of predictions of sound particle acceleration. This was calculated via Euler's equation using a numerically calculated acoustical pressure gradient.

Numerical calculations of gradients require a compromise to be reached between competing concerns of spatial precision and gradient accuracy. Acoustical gradients change with position so that if a gradient is required at a point, it is necessary that the calculation be made close to that point. However, numerical estimation of gradients requires the acoustical field to be sampled over a finite spatial window. If this window is made too small then field differences may include a significant contribution from numerical rounding errors.

The optimal size for a spatial window to calculate acoustical gradients may be expressed in terms of an average acoustical wavelength, $\bar{\lambda}$, based on the concept of the centroid frequency, $\bar{f}$, calculated using the signal amplitude spectrum as a weighting factor [14], [15].

This approach yielded values of $\bar{\lambda}$ of 9.7 and 13.4 m for sources 1 and 2, respectively. The larger values for source 2 are a consequence of the increased low-frequency content of the signals produced by the larger airguns deployed at the front of the line of sources.

An alternative method of calculating the window size was also tried in which the autocorrelation time of source waveforms was calculated then converted to a spatial length by a scaling factor of c_w. This was observed to give similar results of 9.7 and 10.6 m.

The numerical gradient calculations reported here used a spatial window with extent $\bar{\lambda}/4$ in the *x*-, *y*-, and *z*-directions. This fraction was selected after a sensitivity study in which the window size was varied and the stability of results observed. A cube of points with spacing equal to $\bar{\lambda}/80$ was centered on each receiver location of interest, covering the selected spatial extent, the acoustical pressure was then calculated as a function of time at the resulting 8000 points. The gradient in the *x*-direction was calculated by fitting a first-order polynomial to the pressures at the points, plotted as a function of their *x*-coordinate. Similar procedures yielded the gradients in the *y*- and *z*-directions.

Alternatively, the method of images can be modified to avoid the necessity of numerically calculating spatial gradients of the pressure field. This replaces the numerical spatial derivative with a time derivative, which is advantageous because airgun signal models can simulate signals at arbitrarily small time steps, making the numerical calculation of the time derivative simple and accurate. The foundation of this approach is to substitute (1) into Euler's equation and carry out the spatial derivative analytically, which results in the following equations for the three components of the acceleration vector (see Appendix for derivation)

$$\mathbf{a}_j = \frac{\hat{\mathbf{r}}_{d,j}}{\rho r_{d,j}}\left\{\frac{1}{c_w}\frac{\partial s_j\left(t'_{d,j}\right)}{\partial t'_{d,j}} + \frac{1}{r_{d,j}}s_j\left(t'_{d,j}\right)\right\} - \frac{\hat{\mathbf{r}}_{s,j}}{\rho r_{s,j}}\left\{\frac{1}{c_w}\frac{\partial s_j\left(t'_{s,j}\right)}{\partial t'_{s,j}} + \frac{1}{r_{s,j}}s_j\left(t'_{s,j}\right)\right\}. \quad (2)$$

Here, $t'_{d,j} = t - r_{d,j}/c_w$ is often known as the retarded time and is the time at which a signal arriving at the receiver at time t via the direct path was transmitted by airgun j, and $t_{s,j} = t - r_{s,j}/c_w$ is the retarded time for the signal traveling via the surface-reflected path. $\hat{\mathbf{r}}_{d,j}$ is the unit vector in the direction from airgun j to the receiver, and $\hat{\mathbf{r}}_{s,j}$ is the unit vector in the direction from the surface-reflected image of airgun j to the receiver.

C. Wavenumber Integration Method

The wavenumber integration method for acoustical propagation modeling (also known as the integral transform method) is described in detail in [6, Ch. 4] so only a brief outline is given here. This method applies to range-independent waveguides and uses the separation of variables technique to separate the Helmholtz equation into a differential equation in depth, and a Hankel integral transform in range. The depth equation is solved first (either analytically for simple cases or numerically for more general cases) to give the so-called horizontal wavenumber spectrum, from which the acoustical field is calculated by way of the Hankel transform (HT). The advantages of this method are that it can accurately deal with both sea-surface and seabed reflections and that modeled seabeds can range in complexity from simple fluid half-spaces through to arbitrary stacks of fluid and elastic layers.

The wavenumber integration solution is theoretically exact, but the practicalities of its numerical evaluation introduce some errors. In particular, it is common practice to use an exponential approximation to the Hankel function that allows the HT to be evaluated by way of a fast Fourier transform (FFT), greatly speeding up the calculation of the acoustical field. Computer codes that use this approximation are often referred to as fast-field programs. This approximation converges rapidly as range increases but is inaccurate at ranges of the order of an acoustical wavelength. Since this may be significant with respect to the distances outlined in the test cases, the comparison between FFT and HT results is a topic of interest here.

Two implementations of the wavenumber integration method were used to generate the results presented in this paper. Both used SCOOTER [16] to solve the depth equation, and the first used its companion program FIELDS to calculate the acoustical field using the exponential approximation to the Hankel function. The second implementation used a version of FIELDS that had been modified by the authors to use an exact HT for the field calculation. These are referred to in the results section of this paper as the FFT and HT implementations, respectively.

Because the wavenumber integration method is based on the Helmholtz equation, it calculates the acoustical field one frequency at a time. When modeling a broadband source such as an airgun it is therefore necessary to run the program many times to build up the complex transfer function between the source and receiver and then use Fourier synthesis [6] to simulate the received waveform.

The results presented in this paper were computed using a frequency spacing of 1 Hz over the interval 1 to 2000 Hz. Receivers were spaced 0.3 m in depth and 0.35 and 0.33 m in range for the FFT and HT implementations, respectively, and 0.3 m in depth for both implementations. The slightly different range resolutions were required to minimize interpolation errors when interpolating onto the output grids, which were constrained by having different maximum output ranges of 3.5 km and 100 m for the FFT and HT cases, respectively.

wavenumber sampling in SCOOTER is determined indirectly by specifying the minimum and maximum horizontal phase speeds, $c_{\min}$ and $c_{\max}$, and a maximum range, $r_{\max}$. The corresponding horizontal wavenumber integration range is then $k_{\min}$ to $k_{\max}$ where $k_{\min} = \omega/c_{\max}$, $k_{\max} = \omega/c_{\min}$ and ω is the angular frequency. The transform relationship between the spatial and wavenumber domains results in a wavenumber spacing of $\delta k = \pi/r_{\max}$, and an output calculation range grid spacing $\delta r = 2\pi/k_{\max} = c_{\min}/f$ where f is the frequency. The output grid range limits and resolution are specified when running FIELDS by specifying the minimum and maximum ranges and the number of grid points required.

The FFT and HT results presented here were calculated using frequency dependent minimum phase speeds of $0.35f$ and $0.333f$ respectively to achieve calculation range resolutions of 0.35 and 0.33 m. In both cases, the maximum phase speed was set to 10^9 m/s to include energy propagating very close to the vertical.

Experience using SCOOTER has shown that best results are achieved by setting $r_{\max}$ equal to at least double the maximum range at which the transmission loss is to be calculated, but for short range runs this can still result in an undesirably coarse sampling of the wavenumber domain. The algorithm used for determining this parameter was $r_{\max} = \max(2r_m, 2000\delta r)$ where r_m is the maximum output grid range. This led to values of $r_{\max}$ of 7 km and 666 m for the Fourier transform and HT cases, respectively.

The range and depth components of the particle acceleration due to each gun in the array were calculated from the simulated waveforms, with spatial pressure gradients approximated by numerical derivatives calculated by using first-order central finite differences [17]. The range component of the acceleration vector was resolved into X and Y components and each component of the acceleration vector was then summed over the guns in the array.

V. Results

A. Source 1

1) Pressure: Fig. 2 shows sound pressure versus time for source 1 using the two propagation methods considered and calculated for a receiver at a depth of 15 m at x = 3 m, y = 0. In the upper panel, the pressure predicted by the Fourier transform (FFT) method is plotted alongside the result of the image method (IM). Both curves show zero sound pressure at times less than the ~7 ms travel time taken for sound to go from the airgun to the receiver. Both methods predict pressure to rise rapidly after this time but the FFT results show a more rapid rise to a higher peak value. This is emphasized in Fig. 3 where only the earliest times are shown.

The black line marked top and bottom with diamond symbols in Figs. 2 and 3, shows the arrival time of the surface-reflected path. Both curves show a rapid decrease of pressure with time as this negative pressure partially cancels out the positive pressure of the direct-path contribution. At around 53 ms, Fig. 2 shows the arrival of the bottom-bounce path, closely followed by the surface-bottom path at around 60 ms. Both these paths are absent from the IM results and the changes in pressure associated with them are present only in the FFT and HT results. At times

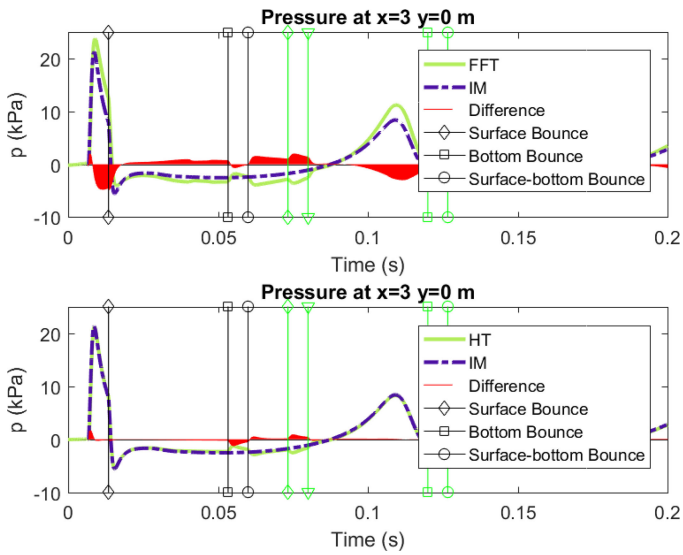

Fig. 2. Sound pressure versus time at $(x, y, z) = (3, 0, 15)$ m due to source 1. Upper panel compares IM (IM, dash–dot curve) with Fourier-transform results (FFT, dark green curve). Lower panel compares IM (IM, dash–dot curve) with full HT results (HT, dark green curve). Vertical lines mark times at which boundary reflections arrive. Green vertical lines show arrivals of multipaths with an additional bottom bounce. Triangles show arrival of surface–bottom–surface path.

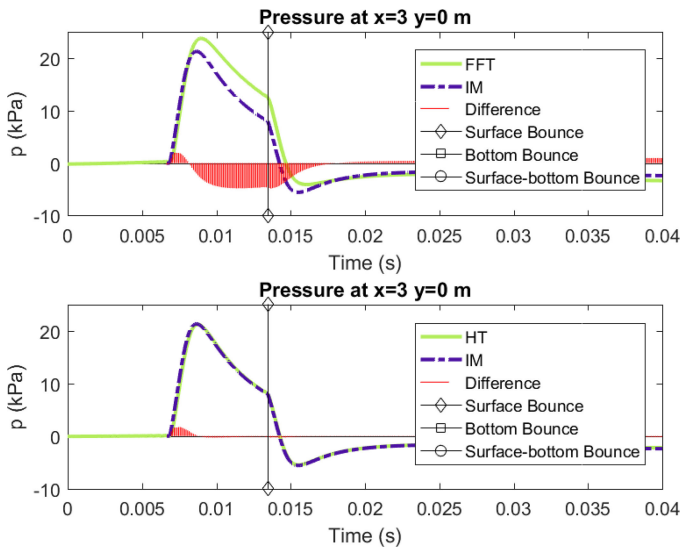

Fig. 3. Sound pressure versus time for a receiver at (3, 0, 15) m in the presence of source 1. Only earliest times are shown. Upper panel compares IM (IM, dash–dot curve) with Fourier-transform results (FFT, dark green curve). Lower panel compares IM (IM, dash–dot curve) with full HT results (HT, dark green curve).

around 100 ms the pressure climbs to a positive peak as a result of the collapse and re-expansion of the air bubble after its first oscillation. In the vicinity of this peak, the agreement between IM and FFT is similar to that observed for the first peak.

The lower panels in Figs. 2 and 3 show a comparison between the IM and HT results. Here, the agreement between the two sets of predictions is excellent with line-on-line matching until the arrival of later multipaths that are excluded from the IM results.

These results indicate that the HT approach provides a reference solution to the propagation wave equation for the case

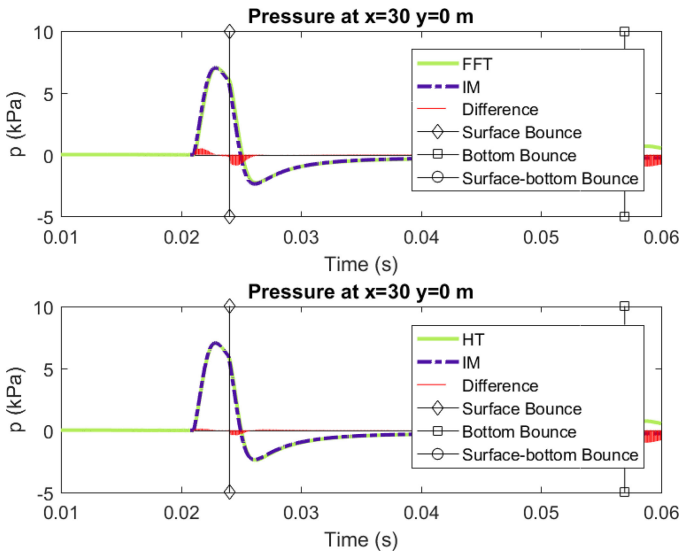

Fig. 4. Pressure time series for a receiver at (30, 0, 15) for source 1. Upper panel compares IM (IM, dash–dot curve) with Fourier-transform results (FFT, dark green curve). Lower panel compares IM (IM, dash–dot curve) with full HT results (HT, dark green curve).

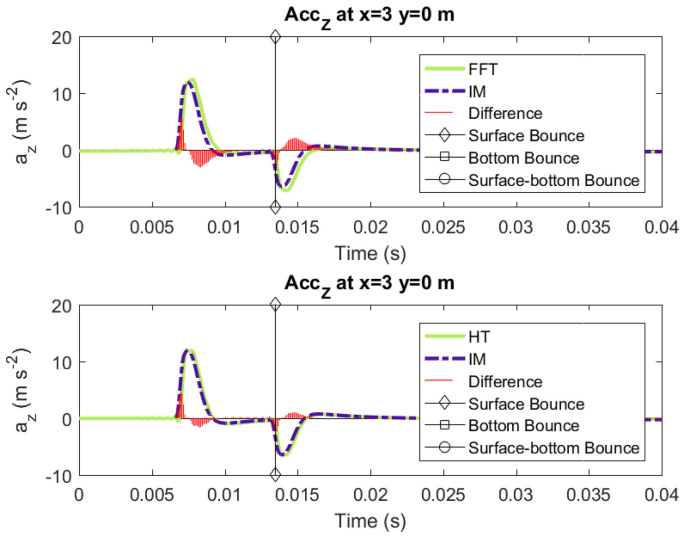

Fig. 5. Particle acceleration in the vertical direction versus time at $(x, y, z) = (3, 0, 15)$ due to source 1. Upper panel shows comparison of method of images with Fourier-transform results. Lower panel compares IM with HT results. Vertical lines mark times at which boundary reflections arrive.

of the receiver at (3, 0, 15) m in the test-case environment with source 1. The IM approach is also accurate before the first bottom reflected arrival. The disagreement between the FFT results and the other two solutions suggests that the exponential approximation to the Hankel function is not valid in this case, almost certainly because of the short ranges considered (the receiver is a fraction of an average wavelength from the source).

Fig. 4 shows pressure time series for a receiver at (30, 0, 15), i.e., at approximately ten times the distance from the source. The increased distance results in closer agreement between the FFT and the other two results.

2) Particle Acceleration: Fig. 5 shows particle acceleration in the vertical direction, calculated for the receiver at (3, 0, 15) m

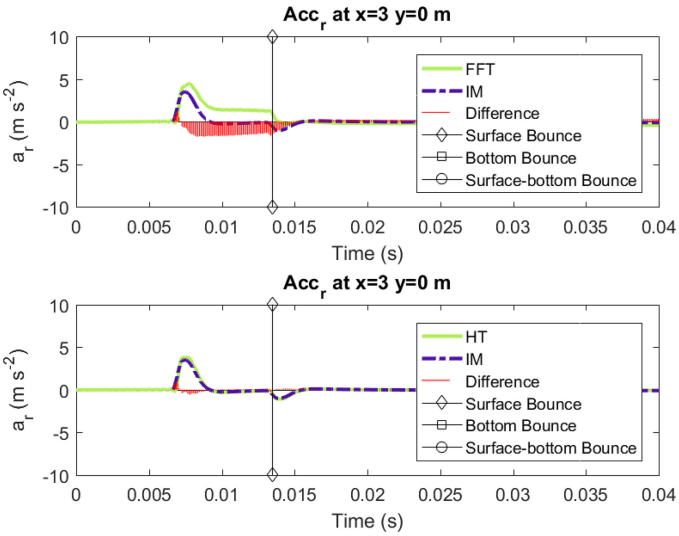

Fig. 6. Particle acceleration in the radial direction versus time at $(x, y, z) = (3, 0, 15)$ due to source 1. Upper panel shows comparison of method of images with Fourier-transform results. Lower panel compares IM with HT results. Vertical lines mark times at which boundary reflections arrive.

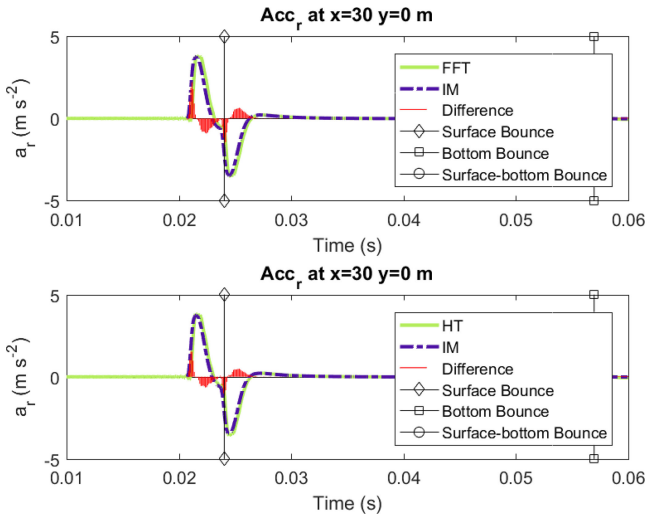

Fig. 7. Particle acceleration in the radial direction versus time at $(x, y, z) = (30, 0, 15)$ due to source 1. Upper panel shows comparison of method of images with Fourier-transform results. Lower panel compares IM with HT results. Vertical lines mark times at which boundary reflections arrive.

in the presence of the single airgun source 1. The acceleration is shown to rise rapidly from zero, reaching a positive peak approximately 1 ms after the first arrival. This positive peak represents a downward acceleration of the water elements, driven by the arrival from above of the pressure wave from the airguns. The passage of the peak of the direct path changes the sign of the pressure gradient as the peak moves below the receiver and the water elements feel a net upward force, resulting in negative acceleration. The magnitude of this negative acceleration decreases with time as the peak of the pressure wave moves further below the receiver but the arrival of the pressure-inverted surface-reflected wave pushes the particle acceleration into a deep trough. This changes with time in a mirror-image of the passage of the direct wave and the particle acceleration then dies out steadily with time until at later times, beyond the scales of Fig. 5, the signal due to the first bubble collapse arrives.

Both panels show reasonable agreement between the IM, FFT, and HT methods with the main differences arising in the peaks and troughs. Close inspection of the HT and FFT data shows small oscillations in the acceleration predicted for times earlier than the arrival of the direct path. Since there is no possible physical cause of these features, they are most likely caused by numerical effects associated with the transforms employed in the HT and FFT methods.

Fig. 6 shows particle acceleration in the radial direction for a receiver at (3, 0, 15) in the presence of source 1. The lower panel shows features similar to those already discussed for the vertical acceleration but the amplitudes of the radial acceleration are generally lower because the line joining source and receiver is at an angle of approximately 73.3° to the horizontal and the majority of particle motion is therefore oriented vertically. The upper panel shows that the FFT method is not producing reliable results for this situation. The decrease in acceleration after the passage of the peak of the direct path is not large enough and the acceleration remains positive, i.e., away from the source, even after the pressure gradient should be driving water molecules back towards the source. This problem is another manifestation of the FFT method's inapplicability to short ranges where the exponential approximation to the Hankel function is not valid.

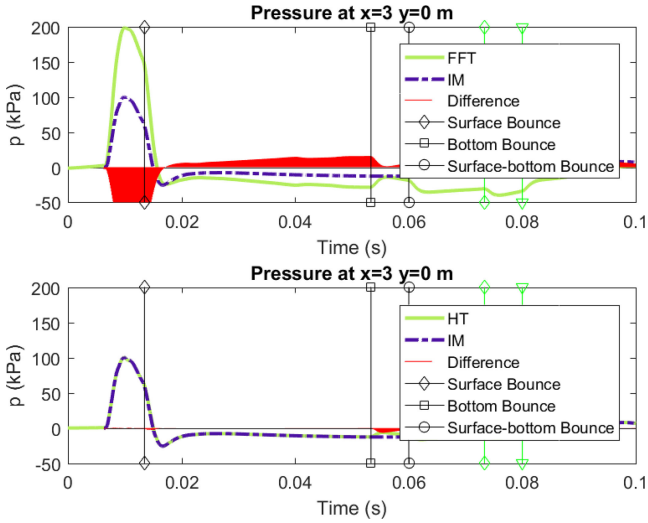

Fig. 8. Pressure versus time at $(x, y, z) = (3, 0, 15)$ m due to source 2. Upper panel shows comparison of method of images with Fourier-transform results. Lower panel compares IM with HT results. Vertical lines mark times at which boundary reflections arrive. Green vertical lines show arrivals of multipaths with an additional bottom bounce.

Fig. 7 shows radial acceleration for a receiver 30 m from source 1. In this case, the HT and FFT methods produce very similar results and the validity of the exponential approximation to the Hankel function is not in question.

B. Source 2 (Case 03)

1) Pressure: Fig. 8 shows pressure time series in the same format as for preceding cases for a receiver at a distance of 3 m along the x-axis. In the figure, the vertical lines show the arrival

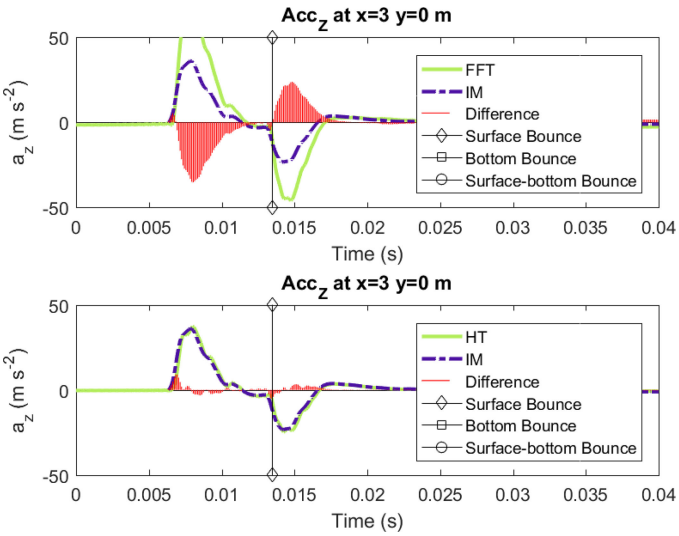

Fig. 9. Particle acceleration in the vertical direction versus time at $(x, y, z) = (3, 0, 15)$ due to source 2. Upper panel shows comparison of method of images with Fourier-transform results. Lower panel compares IM with HT results. Vertical lines mark times at which boundary reflections arrive.

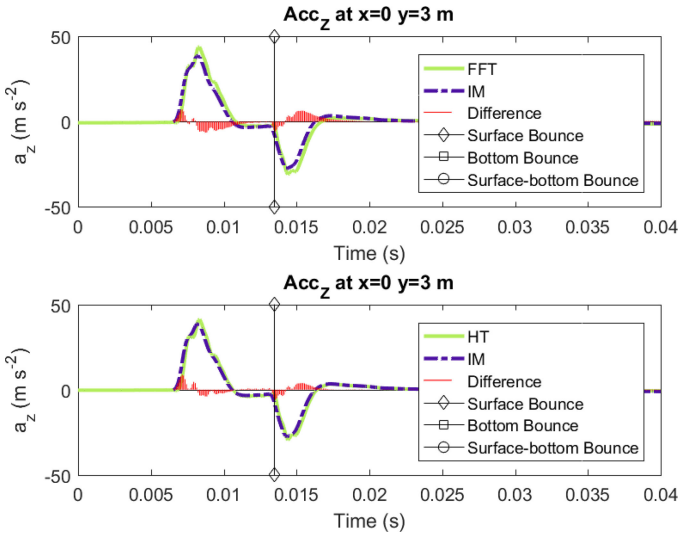

Fig. 10. Particle acceleration in the vertical direction versus time at $(x, y, z) = (0, 3, 15)$ due to source 2. Upper panel shows comparison of method of images with Fourier-transform results. Lower panel compares IM with HT results. Vertical lines mark times at which boundary reflections arrive.

times of multipaths at the receiver from the source at (0,0,5) m. Arrivals from all the airguns in the array will be slightly spread around these times because of the different airgun positions.

The trends in results are similar to the case for source 1 with very good agreement between the HT and IM results and an overestimation of the pressure by the FFT results. Slight disagreements are observed between HT and IM results at around peak pressures but after this, further disagreements are restricted to times at which bottom-reflected multipaths are present.

The results for source 2 show consistent small differences between the IM and HT results that were not as pronounced for source 1. This suggests that there are small phase differences between the two models in the source 2 case that were not present in the source 1 case. This most likely results from a complex-plane interpolation that is required at each frequency to calculate the transfer function at the required receiver location from the regularly spaced (in range) output of the wavenumber integration program. This interpolation is not present for source 1 because, for a single source, the output range grid can be chosen so that the receiver lies on a grid point, but it is impossible to do this simultaneously for all guns in an array. Consequently, small phase differences arise for source 2.

2) Particle Acceleration: Fig. 9 shows vertical particle acceleration for a receiver at (3, 0, 15) in the presence of source 2. The FFT results are shown to overestimate acceleration relative to the IM and HT cases which agree closely. The exponential approximation employed by the FFT method is particularly challenged in this situation because the receiver is directly below one of the airguns in source 2 so that the horizontal offset is zero. Similar problems are not observed in Fig. 10 where the results for the receiver at (0, 3, 15) are shown. Although this receiver has the same offset, it is oriented perpendicular to the array axis so that no source is directly above the receiver. The FFT results are shown to be very similar to the HT and IM results, despite the small horizontal offset. The HT and IM results

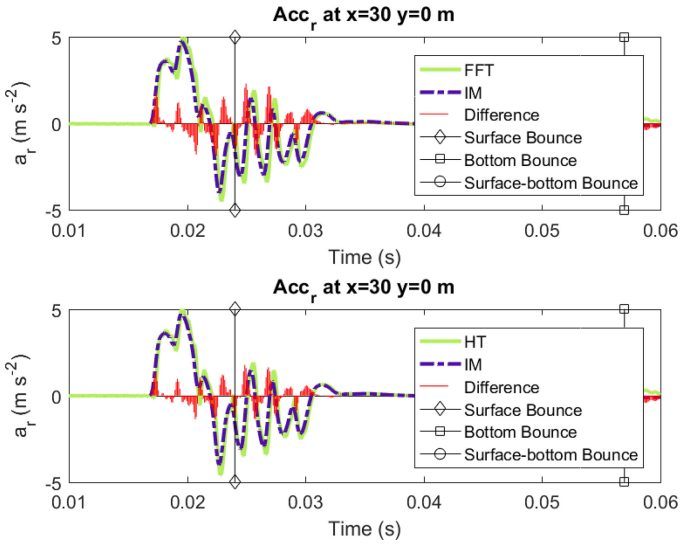

Fig. 11. Particle acceleration in the radial direction versus time at $(x, y, z) = (30, 0, 15)$ due to source 2. Upper panel shows comparison of method of images with Fourier-transform results. Lower panel compares IM with HT results. Vertical lines mark times at which boundary reflections arrive.

in both cases show curve shapes similar to the results already discussed for source 1. Differences occur in that acceleration moduli are higher because of the increased volume of the airgun sources and the curve shows some small-scale structure arising from interference between the contributions of the six airguns. Similar results are observed for the receiver at $(-3, 0, 15)$.

Fig. 11 shows radial acceleration for a receiver at (30, 0, 15) in the presence of source 2. In the context of this extended source, "radial acceleration" indicates "acceleration horizontally away from the origin" and, for this receiver on the x-axis, radial acceleration is synonymous with acceleration in the x-direction.

All three methods show good agreement and the curves show a complicated pattern with rapid oscillations of acceleration with time as the contributions from the six airguns interfere before the arrival of the surface-reflected wave. After this arrival, the oscillations continue, with the sign of the acceleration changing repeatedly. The main differences between the IM and transform results occur in the peaks and troughs where the spatial smoothing of the IM cases results in slight differences with the predictions of the transform-based methods.

VI. Summary

Comparisons between the Fourier transform and HT versions of the wavenumber integration method show that the more approximate Fourier transform form is inaccurate at the shortest ranges considered here. Predictions of pressure made by the exponential method disagree with those made using the full HT and with the method of images. Agreement between these latter two is indicative that they are both valid, given that they are based on very different derivations and it is unlikely that they would both make the same error and predict the same, erroneous values.

Comparison between the method of images and HT results from the wavenumber integration method can be excellent with "line-on-line" agreement possible. Agreement is only observed in the absence of bottom-bounce paths that are not included in the sum over images which considers only direct and surface-reflected paths. This restricts model agreement to short ranges and short times after transmission, i.e., before sound has had time to travel to the seabed and return to the receiver. This restriction might be overcome with a more sophisticated method of images including bottom reflections and multiple surface-bottom interactions.

Good agreement between models is more easily achievable in sound pressure than in particle acceleration. This is partly due to the finite-difference scheme used to calculate pressure gradients needed to predict particle acceleration. Intermodel agreement is hardest to achieve in regions of peaks and troughs of particle acceleration, i.e., where the absolute value of acceleration is highest.

VII. Conclusion

The method of images provides a useful reference solution for propagation at short ranges from arrays of marine-seismic airguns. It can be compared with the results of more sophisticated models and, since it is extremely simple and its approximations are explicit, a sophisticated model agreeing with its predictions may be considered to have been at least partially verified.

The exponential version of the HT used in some wavenumber integration methods is not capable of reproducing the (near-identical) results of the method of images and wavenumber integration methods using the full HT. This is because the exponential version represents a far-field approximation to the HT that is unsuitable for use at the shortest ranges considered.

The short-range results reported here provide a reference point for comparisons of other propagation modeling methods. These comparisons may be in terms of sound pressure and particle acceleration but it should be remembered that the acceleration waveforms can straightforwardly be integrated to give particle velocity or displacement. These measures of particle motion may be the basic output of other modeling methods whose validity is under study. Also, they may be the metrics of particle motion that are more relevant to the study of the acoustical impact of marine-seismic airguns on particular species.

Appendix
Derivation of the Analytic Form of the Particle Acceleration Due to a Point source That Emits an Arbitrary Waveform, and Its Surface-Reflected Image

Define the position vector of the receiver relative to airgun j as $\mathbf{r}_{d,j}$, $\hat{\mathbf{r}}_{d,j}$ as the corresponding unit vector and $r_{d,j} = |\mathbf{r}_{d,j}|$. Substituting the first term in (1) into Euler's equation, gives the contribution of the direct path signal from airgun j to the particle acceleration at the receiver

$$\mathbf{a}_{d,j} = \frac{-1}{\rho} \nabla \left[\frac{s_j\left(t'_{d,j}\right)}{r_{d,j}} \right]. \tag{3}$$

Here, $t'_{d,j} = t - r_{d,j}/c_w$ is the so-called retarded time for the direct path.

Using a local spherical polar coordinate system centered on the airgun and recognizing that for a point source the only nonzero acceleration component is in the radial direction, (3) becomes

$$\mathbf{a}_{d,j} = \frac{-1}{\rho} \frac{\partial}{\partial r_{d,j}} \left[\frac{s_j\left(t'_{d,j}\right)}{r_{d,j}} \right] \hat{\mathbf{r}}_{d,j}. \tag{4}$$

Applying the quotient rule gives

$$\mathbf{a}_{d,j} = \frac{-1}{\rho r_{d,j}} \left\{ \frac{\partial s_j\left(t'_{d,j}\right)}{\partial r_{d,j}} - \frac{s_j\left(t'_{d,j}\right)}{r_{d,j}} \right\} \hat{\mathbf{r}}_{d,j}. \tag{5}$$

Using the chain rule

$$\frac{\partial s_j(t'_{d,j})}{\partial r_{d,j}} = \frac{\partial s_j(t'_{d,j})}{\partial t'_{d,j}} \frac{\partial t'_{d,j}}{\partial r_{d,j}} = -\frac{1}{c_w} \frac{\partial s_j(t'_{d,j})}{\partial t'_{d,j}}.$$

Substituting into (5) gives

$$\mathbf{a}_{d,j} = \frac{\hat{\mathbf{r}}_{d,j}.}{\rho r_{d,j}} \left\{ \frac{1}{c_w} \frac{\partial s_j\left(t'_{d,j}\right)}{\partial t'_{d,j}} + \frac{1}{r_{d,j}} s_j\left(t'_{d,j}\right) \right\}. \tag{6}$$

Carrying out the same procedure starting with the second term in (1) gives the acceleration due to the surface-reflected signal, and adding the accelerations due to the two paths gives (2).

References

[1] A. Mattsson, G. Parkes, and D. Hedgeland, "Svein vaage broadband airgun study," in *The Effects of Noise on Aquatic Life*. New York, NY, USA: Springer, 2012, pp. 469–471.

[2] A. M. Tashmukhambetov *et al.*, "The source characterization study 2007: A detailed three dimensional acoustic field measurement of a seismic airgun array," *J. Acoust. Soc. Amer.*, vol. 124, no. 4, pp. 2599–2599, 2008.

[3] M. A. Ainslie, "Validation of sonar performance assessment tools: A workshop held in memory of David E. Weston, 7–9 April 2010," in *Proc. Inst. Acoust.* 2010, vol. 32, pp. 1–185.

[4] S. Lippert *et al.*, "COMPILE—A generic benchmark case for predictions of marine pile-driving noise," *IEEE J. Ocean. Eng.*, vol. 41, no. 4, pp. 1061–1071, Oct. 2016.

[5] M. A. Ainslie *et al.*, "Verification of airgun sound field models for environmental impact assessment," in *Proc. Meet. Acoust. 4ENAL*, 2016, vol. 27, no. 1, Paper 070018.
[6] F. B. Jensen, W. A. Kuperman, M. B. Porter, and H. Schmidt, *Computational Ocean Acoustics*. New York, NY, USA: Springer, 2011, ch. 4.
[7] A. D. Hawkins, "The hearing abilities of fish," in *Hearing and Sound Communication in Fishes*. New York, NY, USA: Springer, 1981, pp. 109–137.
[8] M. A. Ainslie, R. M. Laws, and H. Ö. Sertlek, "International Airgun Modelling Workshop: Validation of source signature and sound propagation models—Dublin (Ireland), July 16, 2016—Problem description," *IEEE J. Ocean. Eng.*, vol. 44, no. 3, pp. 565–574, Jul. 2019.
[9] W. H. Thorp, "Analytic description of the low-frequency attenuation coefficient," *J. Acoust. Soc. Amer.*, vol. 42, p. 1, 1967.
[10] *Underwater Acoustics—Terminology*, ISO 18405, ISO, Geneva, Switzerland, 2017.
[11] H. Ö. Sertlek and M. A. Ainslie, "Airgun source model (AGORA): Its application for seismic surveys sound maps in the Dutch North Sea," in *Proc. Conf. UAC*, 2015, pp. 439–446.
[12] I. Tolstoy and C. S. Clay, *Ocean Acoustics – Theory and Experiment in Underwater Sound*. College Park, MD, USA: Amer. Inst. Phys., 1987, ch. 5.
[13] L. M. Brekhovskikh and O. A. Godin, *Acoustics of Layered Media II – Point Sources and Bounded Beams*. New York, NY, USA: Springer-Verlag, 1992, ch. 1.
[14] Y. Quan and J. M. Harris, "Seismic attenuation tomography using the frequency shift method," *Geophysics*, vol. 62, no. 3, pp. 895–905, 1997.
[15] L. Liu, J. W. Lane, and Y. Quan, "Radar attenuation tomography using the centroid frequency downshift method," *J. Appl. Geophys.*, vol. 40, no. 1–3, pp. 105–116, 1998.
[16] M. B. Porter, "Acoustics toolbox," 2015. [Online]. Available: http://oalib.hlsresearch.com/FFP/index.html
[17] G. D. Smith, *Numerical Solution of Partial Differential Equations*. London, U.K.: Oxford Univ. Press, 1975, ch. 1.

Mark K. Prior received the B.Sc. degree in physics from the University of Birmingham, Birmingham, U.K., in 1988, and the Ph.D. degree in underwater acoustics from the Institute of Sound and Vibration Research, University of Southampton, Southampton, U.K., in 1996.

He studied many aspects of sonar performance modeling while working at the Admiralty Research Establishment, Portland, U.K., and SACLANTCEN (now CMRE), La Spezia, Italy. Between 2007 and 2014, he was with CTBTO, Vienna, Austria, where he was responsible for automatic signal processing strategies applied to the analysis of underwater-acoustic data gathered for the purposes of global nuclear-test-ban-monitoring. He is currently working for TNO, The Hague, The Netherlands, researching sonar performance modeling and the impact of anthropogenic sound on the marine environment.

Alexander (Alec) J. Duncan (M'92) was born in Melbourne, Australia, in 1958. He received the B.App.Sc. degree in applied physics from the Royal Melbourne Institute of Technology, Melbourne, VIC, Australia, in 1979, the M.App.Sc. degree in applied physics (underwater acoustics) and the Ph.D. degree in underwater acoustics from Curtin University, Perth, WA, Australia, in 1988 and 2004, respectively.

From 1979 to 1980, he was a Development Engineer with Marconi Avionics, Basildon, U.K., and from 1980 to 1984, he was a Research Officer at the University of Bath, Bath, U.K. From 1980 to 1987, he was a Research Assistant at the Western Australian Institute of Technology (now Curtin University). From 1987 to 1991, he was with Internode Pty., Ltd., Melbourne, VIC, Australia, after which he moved back to Curtin University, where he has worked in a number of different roles. He currently holds two positions at the university, where he is a Senior Research Fellow in the Centre for Marine Science and Technology and a Senior Lecturer at the Department of Physics and Astronomy.

Dr. Duncan is a Member of the Acoustical Society of America and the Australian Acoustical Society.

H. Özkan Sertlek received the B.Sc. degree in electronic engineering and the M.S. degree in underwater acoustic propagation from the Department of Gebze Technical University, Gebze, Turkey, in 2006 and 2008, respectively, and the Ph.D. degree in bioacoustics from the University of Leiden, Leiden, The Netherlands, in 2016.

Between 2006 and 2011, he was a Senior Researcher with the Technical Research Council of Turkey (TUBITAK). In summer 2009, he was a Research Fellow with NATO Undersea Research Center. He is currently a Postdoctoral Researcher with the Delphi Consortium, Delft University of Technology, Delft, The Netherlands. His scientific interests include underwater acoustic propagation methods, sound mapping for the environmental risk assessment, and seismic sound source modeling.

Michael A. Ainslie received the B.Sc. degree in physics from Imperial College London, London, U.K., in 1981, and the B.A. degree in mathematics from the University of Cambridge, Cambridge, U.K., in 2011, and the Ph.D. degree in seabed acoustics from the University of Southampton, Southampton, U.K., in 1991.

He is currently a Senior Scientist with JASCO Applied Research, Eschborn, Germany, and a Visiting Professor with the Institute of Sound and Vibration Research, University of Southampton, Southampton, U.K. He is Convenor of the ISO Working Group ISO/TC 43/SC 3/WG 2 (underwater acoustical terminology), and a founding member of the EU expert group Technical Group Noise. He has authored the book *Principles of Sonar Performance Modeling* (Springer, 2010). His research interests include sonar performance modeling and effects of sound on aquatic life.